Applied Physics Letters

Dark-current reduction accompanied photocurrent enhancement in p-type MnO quantum-dot decorated n-type 2D-MoS_2-based photodetector

Cite as: Appl. Phys. Lett. **116**, 112102 (2020); https://doi.org/10.1063/1.5143578
Submitted: 25 December 2019 . Accepted: 02 March 2020 . Published Online: 16 March 2020

Y. Pak, S. Mitra, N. Alaal, B. Xin, S. Lopatin, D. Almalawi, J.-W. Min, H. Kim, W. Kim, G.-Y. Jung, and I. S. Roqan

Applied Physics Letters ARTICLE scitation.org/journal/apl

Dark-current reduction accompanied photocurrent enhancement in p-type MnO quantum-dot decorated n-type 2D-MoS_2-based photodetector

Cite as: Appl. Phys. Lett. **116**, 112102 (2020); doi: 10.1063/1.5143578
Submitted: 25 December 2019 · Accepted: 2 March 2020 ·
Published Online: 16 March 2020

Y. Pak,[1,2] S. Mitra,[1] N. Alaal,[1] B. Xin,[1] S. Lopatin,[3] D. Almalawi,[1,4] J.-W. Min,[5] H. Kim,[2] W. Kim,[2] G.-Y. Jung,[2,a)] and I. S. Roqan[1,a)]

AFFILIATIONS

[1]Physical Sciences and Engineering Division, King Abdullah University of Science and Technology (KAUST), Thuwal 23955-6900, Saudi Arabia
[2]School of Materials Science and Engineering, Gwangju Institute of Science and Technology (GIST), Gwangju 500-712, South Korea
[3]King Abdullah University of Science and Technology (KAUST), Imaging and Characterization core laboratory, Thuwal 23955-6900, Saudi Arabia
[4]Physics Department, Faculty of Science, Taif University, 21974 Taif, P. O. Box 888, Saudi Arabia
[5]King Abdullah University of Science and Technology (KAUST), Computer Electrical Mathematical Science and Engineering, Thuwal 23955-6900, Saudi Arabia

[a)]**Authors to whom correspondence should be addressed:** gyjung@gist.ac.kr and iman.roqan@kaust.edu.sa

ABSTRACT

A highly crystalline single- or few-layered 2D-MoS_2 induces a high dark current, due to which an extremely small photocurrent generated by a few photons can be veiled or distorted. In this report, we show that suppression in the dark current with the enhancement in the photocurrent of a 2D-based photodetector, which is a prerequisite for photoresponse enhancement, can be achieved by constructing an ideal p-n junction based on functionalizing n-type 2D-MoS_2 with p-type quantum dots (QDs). Highly crystalline solution-processed manganese oxide QDs (MnO QDs) are synthesized via the pulsed femtosecond laser ablation technique in ethanol. The ablated MnO QDs are spray-coated on an exfoliated 2D-MoS_2 substrate with interdigitated Au electrodes through N_2-assisted spraying. In the resulting MnO QD-decorated 2D-MoS_2 photodetector with a heterojunction, dark current is reduced and is accompanied by photocurrent enhancement, thereby markedly improving the photoresponsivity and detectivity of MoS_2-based devices. To elucidate the underlying mechanisms contributing to this enhancement, power- and wavelength-dependent photoresponses, along with material characterizations based on spectroscopic, chemical, morphological measurements, and analyses, are discussed.

Incorporating heterojunction architecture into photodetectors (PDs) based on two-dimensional (2D)-transition metal dichalcogenides (TMDCs) can efficiently enhance their photoresponse characteristics. In recent years, 2D molybdenum disulfide (MoS_2) has attracted great attention in the field of optoelectronics, due to its superior electrical, optical, and mechanical characteristics.[1–4] Its layer-dependent physical properties[5–7] such as the bandgap, work function, and energy dispersion relation, in particular, have increased the likelihood of obtaining an ideal platform for photodetectors, thus overcoming the limits of graphene, such as zero-bandgap and optical transmittance.[8,9] Findings yielded by earlier studies based on single- or few-layered MoS_2 have demonstrated superior photodetection characteristics (e.g., a photoresponsivity of 880 A/W, a photo-gain of 1840, and a detectivity of $\sim 10^{12}$ Jones).[10–13] Hybrid MoS_2 materials have also been studied, aiming to efficiently use their excellent 2D characteristics, such as charge transfer and light-matter interactions.[5] For that purpose, formation of heterojunctions with various nanomaterials, such as carbon nanotubes,[14] graphene,[15] and perovskite thin films,[16] was attempted. While such structures have the potential to markedly enhance absorption and quantum efficiency properties,

some critical issues must be addressed before they can be used as a platform for developing hybrid 2D-MoS_2 photodetectors. In general, highly crystalline single- or few-layered 2D-MoS_2 induces a high dark current[11,12] by which an extremely small photocurrent generated by a few photons can be veiled or distorted. Therefore, suppression in the dark current along with the increase in the photocurrent is a prerequisite for photoresponse enhancement (high signal-to-noise ratio), allowing devices to operate at a low light detection limit.

To modulate the dark current, several approaches, such as gate biasing,[10,12,17] molecular physisorption gating,[18] surface modification by plasma ions,[19] and plasmonic hot-electron doping,[20] have been adopted to date. However, all these methods suffer from certain drawbacks; for example, gate biasing requires a third terminal electrode, molecular physisorption is not permanent, and surface modification and hot-electron doping yield unstable results. In addition, 2D-MoS_2 typically occurs in nature as an n-type material although it can exhibit p-type and/or ambipolar properties depending on the metal contact and doping.[21,22] The aforementioned issues can be overcome by constructing the so-called straddling p–n junction between the n-type 2D-MoS_2 and p-type compound semiconducting materials (CSMs), resulting in a higher photoresponse in photodetector devices (compared to MoS_2 Schottky devices) due to a sufficient electron-hole separation via depletion layer.[19,23]

The best p-type material for the ideal straddling p-n heterojunction can be fabricated from CSMs.[24–30] Currently, the fabrication methods of conventional CSM-based devices are expensive and time-consuming and require high-vacuum processes.[31] Moreover, the p-type properties of conventional wide bandgap CSMs such as AlN, ZnO, Ga_2O_3, and Al-rich AlGaN are inadequate because the p-type property of such CSMs is neither readily induced nor stable.[32–36] Thus, very recently, this motivated us to discover p-type wide bandgap CSMs based on manganese oxide (MnO) quantum dots (QDs). Solution-processed p-type CSM-QDs featuring superior 0D properties can be very promising candidates for heterojunction formation with TMDCs due to low-cost synthesis and/or doping and easy integration onto a large area of versatile substrates.[37–39] However, first, the crystallinity of CSM-QDs must be preserved during synthesis and fabrication to ensure stable p-type properties. Second, CSM-QDs need to have a homogeneous volume or size that must be dispersed without aggregation. Finally, to uniformly disperse CSM-QDs and stably deliver photo-signals, a stable 2D material as a heterojunction counterpart is necessary. However, p-n junction (or heterojunction) devices based on n-type 2D TMDCs hybridized with p-type (or n-type) solution-processed QDs have not been investigated yet.

In this work, we demonstrated that the aforementioned issues can be overcome by constructing a p-n junction between the n-type 2D-MoS_2 and p-type QDs. These preconditions were satisfied by producing cost-effective p-n junction devices based on 2D TMDC/0D solution-processed QDs. The laser ablated MnO QDs in liquid were spray-coated on an exfoliated 2D-MoS_2 substrate through N_2-assisted spraying method. The photodetectors with the heterojunction structure between the p-MnO QDs and the exfoliated 2D n-MoS_2 exhibited a reduced dark current and an increased photocurrent, resulting in enhanced photoresponse characteristics.

Femtosecond laser ablation in liquid (FLAL) was carried out to synthesize MnO QDs. A Mn_2O_3 sputtering target (99.9% purity, ALB-Materials, Inc.) was immersed in a quartz glass beaker with ethanol (C_2H_5OH). The target surface was ablated by using a Ti:sapphire (Coherent-Mira 900) femtosecond (fs) laser with a pulse width and repetition rate of 150 fs and 76 MHz, respectively, at a wavelength of 800 nm.[37–39] The beaker was placed on a rotating stage to ensure uniform laser ablation. The ablation duration was ∼1 h at a constant laser power of 1.7 W. A 200 nm-thick silicon oxide (SiO_2)/Si (a heavily doped p-type material) substrate was prepared by transferring the exfoliated MoS_2 on it. After photolithography, metal deposition, and lift-off process, Ti (∼3 nm)/Au (∼70 nm) interdigitated electrodes (IDEs) with a channel length and width of 5 μm and 640 μm were constructed on the exfoliated MoS_2/SiO_2 substrate. Thermal annealing was carried out for 1 h at 100 °C in vacuum to reduce contact resistance at the interface between the IDEs and 2D-MoS_2. The prepared MnO QD solution was spray-coated on the MoS_2/SiO_2 sample by using a nitrogen-assisted spray gun (Fig. 1). During spray-coating, the substrate temperature was maintained at 90 °C by keeping it on a hot plate to rapidly vaporize ethanol, thus minimizing MnO QD aggregation. Note that the spraying time was optimized by monitoring a two-probe electrical resistance to avoid the formation of a complete MnO QD film and/or network throughout the channel.

High-resolution transmission electron microscopy (HR-TEM) and scanning TEM (STEM) measurements were conducted (Titan 60–300 microscope, FEI Corp.) using an electron beam energy of 300 keV. To confirm the material composition, energy dispersive x-ray spectroscopy (EDX) was carried out using the STEM system. X-ray photoelectron spectroscopy (XPS) was performed in a Kratos Axis Supra DLD spectrometer, which generates a monochromatic Al K_α x-ray signal ($h\nu = 1486.6$ eV) under an operating power of 150 W and a vacuum of 1×10^{-9} mbar. Absorbance was measured at room temperature using a UV-Vis Varian Cary 5000 spectrophotometer. Room temperature micro-photoluminescence spectra were excited by a 325 nm He–Cd laser. Both micro-photoluminescence (PL) and Raman measurements were performed using a Horiba Aramis micro-Raman spectrometer. The topography and roughness of the MnO QD film were confirmed using a Bruker atomic force microscopy (AFM) system (MultiMode 8-HR AFM). PD devices were probed and

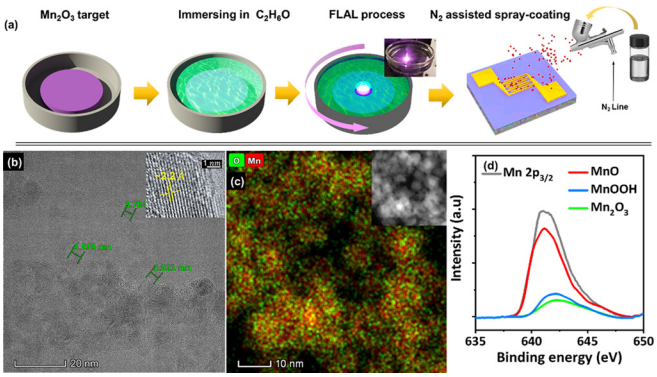

FIG. 1. MnO QD preparation and material characterizations; (a) MnO QD/MoS_2 device fabrication through FLAL and N_2-assisted spray-coating. (b) HR-TEM image of MnO QDs dispersed on a TEM carbon grid. [The inset shows the lattice spacing (∼2.2 Å) for a single QD.] (c) The EDX map (the red color is Mn, and the green one is O) acquired from the area shown in the HAADF-STEM image illustrated in the inset. (d) Compositional characterization of QDs via XPS analysis.

connected to a Keithley 2400S Source Meter, using electrical feedthrough. Changes in electrical resistance were monitored using LabVIEW I−V software. PDs were illuminated by a solar simulator for generating air mass (AM) 1.5 standard solar spectral light, and a monochromator (FLS 980, Edinburgh Instruments) was employed for modulating the light wavelength from 260 nm to 700 nm. The irradiation time was accurately controlled, using an automatic shutter system. To modulate the power density (P_d), neutral-density (ND) filters with different transmittances (40, 25, 15, 10, 1, and 0.1%) were placed underneath the solar simulator shutter emitting a standard calibration P_d of 100 mW/cm^2. Detectivity (D^*), defined as the capability of distinguishing weak signals from noise, was calculated based on the following expression:

$$D^* = \frac{R_{ph}A^{1/2}}{\sqrt{2eI_{dark}}}, \quad (1)$$

where A is the channel area, e denotes the electron charge, and I_{dark} is the dark current, while R_{ph} is the photoresponsivity, which is defined as the ratio of I_{ph} to the incident light power.

Figure 1(a) shows the fabrication process of the MnO QD-decorated 2D-MoS_2 device adopted in the present study. The MnO QDs were synthesized via FLAL, as it is an easy and highly reproducible technique for fabricating well-dispersed QDs without the aid of any surfactant material. More details about the FLAL process have been reported in our previous studies.[37–39] The HR-TEM image [Fig. 1(b)] shows the crystalline MnO QDs with a diameter range < 7 nm.[38] A HR-STEM image of an individual MnO QD shown in the inset of Fig. 1(b) indicates that the QD lattice spacing corresponds to the (200) and (111) atomic planes, respectively.[40] EDX maps [Fig. 1(c)] confirm that the Mn and O atoms were homogeneously distributed within individual MnO QDs [the inset shows the corresponding high-angle annular dark-field (HAADF)-STEM image]. The XPS spectra shown in Figs. 1(d) and S1 (supplementary material) reveal that MnO as a major phase accounted for 81.5% of the QD composition, while the minor phases are MnOOH (12%) and Mn_2O_3 (6.5%), which is in line with the previous findings.[38]

As reported in our recent published work, the p-type property of the MnO QDs has been confirmed by studying the field-effect transistor (FET) characteristics.[38] Theoretically, hybridizing n-type 2D-MoS_2 (hereafter, denoted simply as MoS_2) by p-type MnO QDs forms a p-n junction, inducing charge transfer due to a work function difference that results in a "straddling heterojunction" at the interface. Figure 2(a) shows the Raman spectra of both bare MoS_2 and MnO QD-decorated MoS_2 (MnO QD/MoS_2), measured at a laser excitation wavelength of 473 nm. Two MoS_2 characteristic peaks of E_{2g} and A_{1g}, originating from in-plane and out-of-plane vibration mode, respectively,[41] are clearly visible in the spectra. E_{2g} and A_{1g} of the bare MoS_2 were located at 383.44 cm^{-1} and 408.41 cm^{-1}, respectively, which indicates the existence of multilayered MoS_2. After decoration with MnO QDs, a notable change in the A_{1g}/E_{2g} intensity ratio from 1.77 to 1.87 occurred, which can imply charge transfer through the heterojunction interface.[42–44]

The PL spectra of the samples (without IDEs) shown in Fig. 2(b) and Fig. S2 provide further evidence supporting the charge transfer. Typical A* exciton peaks were found at 1.831 eV and 1.824 eV for bare MoS_2 and MnO QD/MoS_2, respectively,[1] while the PL intensity of MnO QD/MoS_2 emission increased by ∼50% (Fig. S2 shows the PL spectra for the other five sets). In the pertinent literature, high PL intensities were ascribed to positively charged excitons or trions in MoS_2, as QDs provide more carriers.[17,18,45] However, PL has been performed on materials but not on devices, implying that the generated carrier density is enhanced for MnO QD/MoS_2 samples, as the carriers are generated from the two materials (electrons from the n-type and holes from the p-type material), and resulting in a higher carrier generation rate compared to a bare MoS_2, ultimately yielding a higher PL intensity. As there is no external electric field separating the electron−hole pairs, they recombine radiatively.[46–48]

Figure 3(a) displays a schematic diagram of the MnO QD/MoS_2 photodetector (PD) structure, whereas the image shown in Fig. 2(b) confirms the presence of MnO QD/MoS_2 sample between the Au IDEs, with a channel length of 5 μm. The MoS_2 flakes used for PDs ranged in thickness from 5 nm to 20 nm, as confirmed by AFM. A root mean square roughness of individual MoS_2 flakes for the PDs was less than 0.6 nm, as shown in Fig. 3(c). The energy diagrams obtained before and after hybridizing MoS_2 by MnO QDs are shown in Figs. 3(d) and 3(e). Recently, we have found the work function and the Fermi level of these p-MnO QDs using Kelvin probe measurements, (the findings and detailed discussions have been published elsewhere).[38] The work function of the MnO QD film was estimated to be at ∼4.87 V, while its bandgap energy, estimated from the absorption

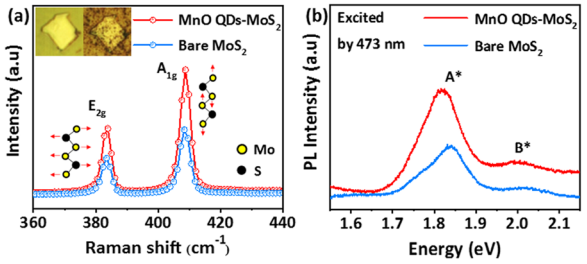

FIG. 2. Spectroscopic analysis of the MnO QD/MoS_2 and bare MoS_2 via (a) Raman and (b) PL measurements. The inset of (a) shows optical microscope images of a MoS_2 sample before (left) and after (right) spray-coating of QDs.

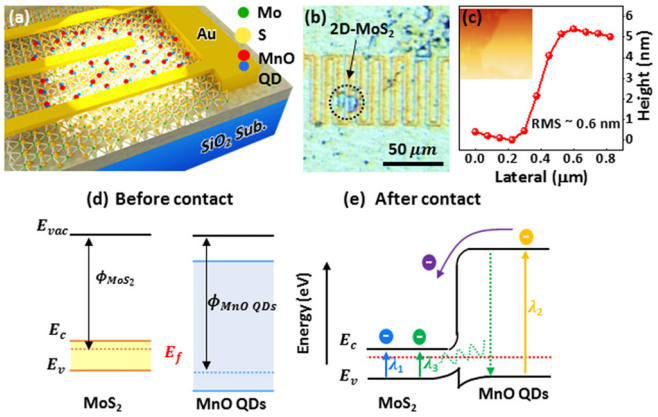

FIG. 3. (a) A schematic of MnO QD/MoS_2 PD. (b) An optical microscope and (c) AFM images of an exfoliated MoS_2 flake placed underneath the IDEs. Energy band diagrams for (d) separated MnO QDs and MoS_2 and (e) after hybridizing MoS_2 by the MnO QDs.

spectra of colloidal MnO QDs in ethanol, is ~5 eV (Fig. S3, supplementary material). The work function and bandgap energy of a 6 nm thick MoS_2 were ~4.8 eV and 1.3 eV, respectively. When the two materials are attached after spray-coating the QDs on MoS_2 [Fig. 3(e)], their respective Fermi energies are aligned and carriers are transferred to the MnO QDs, thereby decreasing the electron conductivity of MoS_2. As the valence band (VB) maximum of the MnO QDs is at the lower energy level than the VB of MoS_2, a cusp discontinuity can be created at the VB junction.

Under illumination, three representative absorption paths (denoted as λ_1, λ_2, and λ_3) can be activated to generate electron–hole pairs. λ_1 and λ_2 are the major photogeneration paths corresponding to the intrinsic bandgap energies of MoS_2 and MnO QDs, respectively. The photogeneration frequency through λ_2 is high enough due to the sufficient hole density around the VB of MnO QDs. Consequently, photogenerated electrons at the conduction band (CB) of MnO QDs can be favorably supplied into MoS_2 by a high junction potential. An alternative absorption path, denoted as λ_3, can exist since the recombination is prone to occur around the VB cusp with many trap states.

Figure 4 shows the performance of both bare MoS_2 and MnO QD/MoS_2 PDs. The dark current (I_{dark}) and photocurrent (I_{ph}) before and after MnO QD decoration were analyzed under irradiation at different voltages, which varied from −1 V to 1 V in 20 mV increments [Fig. 4(a)]. I_{dark} of the MnO QD/MoS_2 PD (e.g., 5 nA) was much smaller than that of the bare MoS_2 PD (e.g., 10 nA) at every voltage. In contrast, under the power density (P_d, defined as the incident light power per unit projected area) of 100 mW/cm^2, I_{ph} of the MnO QD/MoS_2 PD (e.g., 52 nA) was much higher than that of the bare MoS_2 PD (e.g., 32 nA). Figure 4(b) exhibits the cyclic photoresponse of both PDs under the 5 s ON/10 s OFF irradiation cycle. At 0.2 V, both PDs were subjected to different power densities (corresponding to the P_d values of 100, 40, 25, 15, 10, and 1 mW/cm^2). As indicated in Fig. 4(a), the MnO QD/MoS_2 PD produced higher I_{ph} at every P_d, which demonstrates that an enhanced photoresponse was obtained by the PD incorporating the straddling p-n junction. Photoresponse efficiency

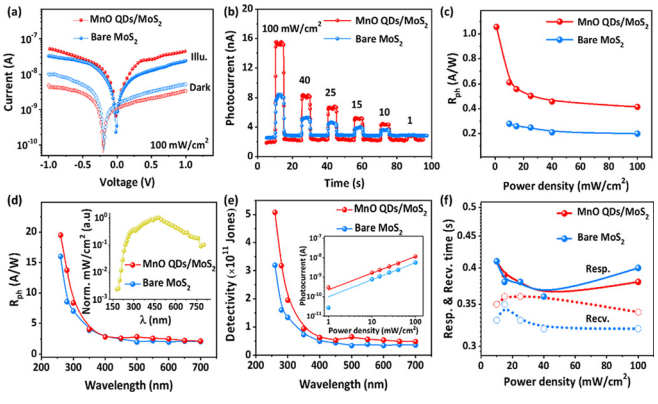

FIG. 4. Enhanced performance of the MnO QD/MoS_2 PD. (a) Current–voltage characteristic of the bare MoS_2 and MnO QD/MoS_2 PDs under dark conditions and 100 mW/cm^2 irradiation. (b) Cyclic photoresponse behaviors and (c) R_{ph} of both PDs at various P_d values. Wavelength-dependent (d) R_{ph} and (e) approximated detectivity. [The inset of (d) shows the normalized P_d values of monochromatic light incident on the PDs and the inset of (e) shows the logarithmic plot of the photocurrent as a function of P_d.] (f) T_{Resp} and T_{recv} as a function of P_d.

was evaluated by calculating R_{ph}. Under 100 mW/cm^2, the MnO QD/MoS_2 PD showed twofold higher R_{ph} [Fig. 4(c)]. At 1 mW/cm^2, R_{ph} of the MnO QD/MoS_2 PD surpassed 1 A/W, while no I_{ph} was observed in the bare MoS_2 PD. Considering a long channel length of 5 μm, which is generally unfavorable for efficient photogeneration by recombination and/or trapping, the achieved I_{ph} increase and the I_{dark} reduction are notable.

To identify the potential factors contributing to the observed R_{ph} increase in QD/MoS_2 PDs, especially in the UV range, as p-MnO QDs have a wide bandgap, operating in the deep UV spectral region, wavelength-dependent photoresponse was analyzed using monochromatic light, whereby the wavelength was increased from 260 nm to 800 nm in 50 nm steps. Interestingly, at 260 nm, the R_{ph} value (~20 A/W) was enhanced for the MnO QD/MoS_2 PD compared to the bare device, as shown in Fig. 4(d). Note that monochromatic light is characterized by different P_d values, as indicated in the inset of Fig. 4(d); hence, it is rational to compare R_{ph} values obtained for the device with and without the MnO QDs at the same wavelength. R_{ph} markedly increased at wavelengths below 300 nm, which is sufficient for generating electron–hole pairs from the wide bandgap MnO QDs. Moreover, the detectivity values of both MnO QD/MoS_2 and bare MoS_2 PDs as a function of wavelength are shown in Fig. 4(e). In line with the increasing R_{ph} trend in MnO QD/MoS_2 PD, the detectivity was markedly enhanced at wavelengths below 300 nm, reaching about 5×10^{11} Jones at $\lambda = 260$ nm as the photoresponse in the UV range below 350 nm is expected to be through λ_3, with only a minor contribution from λ_2.[38] These finding support our hypothesis that some of the photogenerated carriers are delivered from the MnO QDs (as an additional absorber) to MoS_2 (signal-transducing platform). The depletion layer formed at the p-n junction aids in the fast separation of photogenerated carriers,[19] thereby reducing the likelihood of recombination and thus improving the total photocurrent and device photo responsivity compared to that of Schottky devices based on bare MoS_2, as shown in Fig. 4. Based on the band diagram shown in Fig. 3(e), as well as the spectroscopic data, we can expect that this p–n junction can contribute to the dark current decrement while increasing the photocurrent of the MnO QD/MoS_2 PD. The observed decrease in the dark current can also be attributed to the MnO QDs working as the electron blocking layer.

The kinetics of photogeneration and transportation through the junction and/or materials can be indirectly estimated by fitting the relationship between the photocurrent and power density based on the power law equation $I_{ph} = \alpha \cdot P^{\beta}$, where α is a proportionality constant and β is a photosensitivity factor [in the inset of Fig. 4(e)]. The logarithmic-scale sublinear fitting lines yielded a β of 0.87 and 0.85 for the bare MoS_2 PD and the MnO QD/MoS_2 PD, respectively. The slightly reduced β is mainly due to trap states at the junction and the oxygen-related defects[4] and can indicate that the MnO QD exerts negligible influence on the recombination of the photogenerated carriers.

The calculated response (T_{Resp}) and recovery (T_{Recv}) times are shown in Fig. 4(f), which are defined as the time required to reach 90% and attenuate to 90% of the maximum current, respectively, were extracted. For both bare MoS_2 and MnO QD/MoS_2 PDs, T_{Resp} and T_{Recv} below 0.5 s were obtained under every P_d. T_{Recv} values become slightly longer due to the MnO QD decoration, but P_d dependency of either T_{Resp} or T_{Recv} could not be confirmed. This slightly longer recovery time can be due to states in the bandgap that are related to

the MnO QD surface states.[38] In addition, the metal–semiconductor junction can result in different recovery times.[4,49]

In conclusion, highly crystalline p-type MnO QDs were fabricated via pulsed femtosecond laser ablation, which is a low-cost, efficient, and environmentally friendly technique. The dark current of MnO QD/MoS_2 PDs was suppressed due to MnO QD decoration, while the photocurrent markedly increased. The heterojunction contributed to the lower electron conductivity of MoS_2 under dark conditions, while electron–hole pair generation was enhanced through the intrinsic absorption path of the p-type MnO QDs. The method described here can be further explored for facile fabrication of heterojunction devices based on other CSM QDs and 2D-TMDCs to endow them with unique optoelectronic properties.

See the supplementary material for the detailed experimental data on XPS, PL, and absorption spectra.

AUTHOR'S CONTRIBUTIONS

Y. Pak and S. Mitra contributed equally to this work.

The authors thank KAUST for the financial support via base Fund No. BAS/1/1319-01-01.

REFERENCES

[1]K. F. Mak, C. Lee, J. Hone, J. Shan, and T. F. Heinz, Phys. Rev. Lett. **105**, 136805 (2010).
[2]Q. H. Wang, K. Kalantar-Zadeh, A. Kis, J. N. Coleman, and M. S. Strano, Nat. Nanotechnol. **7**, 699 (2012).
[3]Y. Jung, J. Shen, and J. J. Cha, Nano Convergence **1**, 18 (2014).
[4]Y. Pak, W. Park, S. Mitra, A. A. Sasikala Devi, K. Loganathan, Y. Kumaresan, Y. Kim, B. Cho, G.-Y. Jung, M. M. Hussain, and I. S. Roqan, Small **14**, 1870022 (2018).
[5]Z. Y. Zhao and Q. L. Liu, Catal. Sci. Technol. **8**, 1867 (2018).
[6]S. H. Choi, Z. Shaolin, and W. Yang, J. Korean Phys. Soc. **64**, 1550 (2014).
[7]B. Wang, C. Muratore, A. A. Voevodin, and M. A. Haque, Nano Convergence **1**, 22 (2014).
[8]T. Mueller, F. Xia, and P. Avouris, Nat. Photonics **4**, 297 (2010).
[9]Y. Z. Zhang, T. Liu, B. Meng, X. H. Li, G. Z. Liang, X. N. Hu, and Q. J. Wang, Nat. Commun. **4**, 1811 (2013).
[10]Z. Yin, H. Li, H. Li, L. Jiang, Y. Shi, Y. Sun, G. Lu, Q. Zhang, X. Chen, and H. Zhang, ACS Nano **6**, 74 (2012).
[11]O. Lopez-Sanchez, D. Lembke, M. Kayci, A. Radenovic, and A. Kis, Nat. Nanotechnol. **8**, 497 (2013).
[12]M. A. Carignano, S. A. Aravindh, I. S. Roqan, J. Even, and C. Katan, J. Phys. Chem. C **121**, 20729–20738 (2017).
[13]X. Wang, P. Wang, J. Wang, W. Hu, X. Zhou, N. Guo, H. Huang, S. Sun, H. Shen, T. Lin, M. Tang, L. Liao, A. Jiang, J. Sun, X. Meng, X. Chen, W. Lu, and J. Chu, Adv. Mater. **27**, 6575 (2015).
[14]D. Jariwala, V. K. Sangwan, C. C. Wu, P. L. Prabhumirashi, M. L. Geier, T. J. Marks, L. J. Lauhon, and M. C. Hersam, Proc. Natl. Acad. Sci. U. S. A. **110**, 18076 (2013).
[15]D. De Fazio, I. Goykhman, D. Yoon, M. Bruna, A. Eiden, S. Milana, U. Sassi, M. Barbone, D. Dumcenco, K. Marinov, A. Kis, and A. C. Ferrari, ACS Nano **10**, 8252 (2016).
[16]Y. Wang, R. Fullon, M. Acerce, C. E. Petoukhoff, J. Yang, C. Chen, S. Du, S. K. Lai, S. P. Lau, D. Voiry, D. O'Carroll, G. Gupta, A. D. Mohite, S. Zhang, H. Zhou, and M. Chhowalla, Adv. Mater. **29**, 1603995 (2017).
[17]A. K. M. Newaz, D. Prasai, J. I. Ziegler, D. Caudel, S. Robinson, R. F. Haglund, and K. I. Bolotin, Solid State Commun. **155**, 49 (2013).
[18]S. Tongay, J. Zhou, C. Ataca, J. Liu, J. S. Kang, T. S. Matthews, L. You, J. Li, J. C. Grossman, and J. Wu, Nano Lett. **13**, 2831 (2013).
[19]F. Xue, L. Chen, J. Chen, J. Liu, L. Wang, M. Chen, Y. Pang, X. Yang, G. Gao, J. Zhai, and Z. L. Wang, Adv. Mater. **28**, 3391 (2016).
[20]Y. Kang, S. Najmaei, Z. Liu, Y. Bao, Y. Wang, X. Zhu, N. J. Halas, P. Nordlander, P. M. Ajayan, J. Lou, and Z. Fang, Adv. Mater. **26**, 6467 (2014).
[21]X. Liu, D. Qu, J. Ryu, F. Ahmed, Z. Yang, D. Lee, and W. J. Yoo, Adv. Mater. **28**, 2345 (2016).
[22]S. Chuang, C. Battaglia, A. Azcatl, S. McDonnell, J. S. Kang, X. Yin, M. Tosun, R. Kapadia, H. Fang, R. M. Wallace, and A. Javey, Nano Lett. **14**, 1337 (2014).
[23]Y. Lee, Y. Hwang, and Y. C. Chung, ACS Appl. Mater. Interfaces **7**, 7163 (2015).
[24]N. Alfaraj, S. Mitra, F. Wu, I. A. Ajia, B. Janjua, A. Prabaswara, R. A. Aljefri, H. Sun, T. Khee Ng, B. S. Ooi, I. S. Roqan, and X. Li, Appl. Phys. Lett. **110**, 161110 (2017).
[25]W.-Y. Kong, G.-A. Wu, K.-Y. Wang, T.-F. Zhang, Y.-F. Zou, D.-D. Wang, and L.-B. Luo, Adv. Mater. **28**, 10725 (2016).
[26]Y. K. Fang, S. B. Hwang, K. H. Chen, C. R. Liu, M. J. Tsai, and L. C. Kuo, IEEE Trans. Electron Devices **39**, 292 (1992).
[27]R. McClintock, A. Yasan, K. Minder, P. Kung, and M. Razeghi, Appl. Phys. Lett. **87**, 241123 (2005).
[28]J. Li, Z. Y. Fan, R. Dahal, M. L. Nakarmi, J. Y. Lin, and H. X. Jiang, Appl. Phys. Lett. **89**, 213510 (2006).
[29]B. Cheng, T. Y. Li, P. Maity, P. C. Wei, D. Nordlund, K. T. Ho, D. H. Lien, C. H. Lin, R. Z. Liang, X. Miao, I. A. Ajia, J. Yin, D. Sokaras, A. Javey, I. S. Roqan, O. F. Mohammed, and J.-H. He, Commun. Phys. **1**, 1–8 (2018).
[30]Y. Lu, Z. Wu, W. Xu, and S. Lin, Nanotechnology **27**, 48LT03 (2016).
[31]M. Martens, J. Schlegel, P. Vogt, F. Brunner, R. Lossy, J. Würfl, M. Weyers, and M. Kneissl, Appl. Phys. Lett. **98**, 211114 (2011).
[32]H. X. Jiang and J. Y. Lin, Semicond. Sci. Technol. **29**, 084003 (2014).
[33]C. H. Park, S. B. Zhang, and S. H. Wei, Phys. Rev. B **66**, 073202 (2002).
[34]S. J. Pearton, J. Yang, P. H. Cary, F. Ren, J. Kim, M. J. Tadjer, and M. A. Mastro, Appl. Phys. Rev. **5**, 011301 (2018).
[35]Z. Zhang, U. Schwingenschlögl, and I. S. Roqan, RSC Adv. **4**, 50759–50764 (2014).
[36]F. Wu, H. Sun, I. A. AJia, I. S. Roqan, D. Zhang, J. Dai, C. Chen, Z. C. Feng, and X. Li, J. Phys. D: Appl. Phys. **50**, 245101 (2017).
[37]S. Mitra, A. Aravindh, G. Das, Y. Pak, I. Ajia, K. Loganathan, E. D. Fabrizio, and I. S. Roqan, Nano Energy **48**, 551 (2018).
[38]S. Mitra, Y. Pak, N. Alaal, M. N. Hedhili, D. R. Almalawi, N. Alwadai, K. Loganathan, Y. Kumarasan, N. Lim, G. Y. Jung, and I. S. Roqan, Adv. Opt. Mater. **7**, 1900801 (2019).
[39]S. Mitra, Y. Pak, B. Xin, D. R. Almalawi, N. Wehbe, and I. S. Roqan, ACS Appl. Mater. Interfaces **11**, 38921 (2019).
[40]C. Liu, C. Zhang, H. Song, X. Nan, H. Fu, and G. Cao, J. Mater. Chem. A **4**, 3362 (2016).
[41]C. Lee, H. Yan, L. E. Brus, T. F. Heinz, J. Hone, and S. Ryu, ACS Nano **4**, 2695 (2010).
[42]H. Li, Q. Zhang, C. C. R. Yap, B. K. Tay, T. H. T. Edwin, A. Olivier, and D. Baillargeat, Adv. Funct. Mater. **22**, 1385 (2012).
[43]Y. Shi, J. K. Huang, L. Jin, Y. Te Hsu, S. F. Yu, L. J. Li, and H. Y. Yang, Sci. Rep. **3**, 1839 (2013).
[44]A. P. Nayak, S. Bhattacharyya, J. Zhu, J. Liu, X. Wu, T. Pandey, C. Jin, A. K. Singh, D. Akinwande, and J. F. Lin, Nat. Commun. **5**, 3731 (2014).
[45]K. F. Mak, K. He, C. Lee, G. H. Lee, J. Hone, T. F. Heinz, and J. Shan, Nat. Mater. **12**, 207 (2013).
[46]M. M. Muhammed, N. Alwadai, S. Lopatin, A. Kuramata, and I. S. Roqan, ACS Appl. Mater. Interfaces **9**, 34057–34063 (2017).
[47]T. H. Flemban, M. C. Sequeira, Z. Zhang, S. Venkatesh, E. Alves, K. Lorenz, and I. S. Roqan, J. Appl. Phys. **119**, 065301 (2016).
[48]I. A. Ajia, P. R. Edwards, Y. Pak, E. Belekov, M. A. Roldan, N. Wei, Z. Liu, R. W. Martin, and I. S. Roqan, ACS Photonics **5**, 820–826 (2018).
[49]D. Y. Guo1, Z. P. Wu1, Y. H. An, X. C. Guo, X. L. Chu, C. L. Sun, L. H. Li, P. G. Li1, and W. H. Tang, Appl. Phys. Lett. **105**, 023507 (2014).